Journal of
Materials Chemistry C

PAPER

View Article Online
View Journal



Cite this: DOI: 10.1039/c9tc04933a

# The mechanical, electronic and optical properties of two-dimensional transition metal chalcogenides $MX_2$ and $M_2X_3$ (M = Ni, Pd; X = S, Se, Te) with hexagonal and orthorhombic structures†

Wenqi Xiong, [a] Kaixiang Huang [a] and Shengjun Yuan *[ab]

Received 6th September 2019,
Accepted 7th October 2019

DOI: 10.1039/c9tc04933a

rsc.li/materials-c

In this paper, we perform first-principle studies on the mechanical, electronic and optical properties of two-dimensional transition metal chalcogenides $MX_2$ and $M_2X_3$ where M = Ni or Pd and X = S, Se or Te. For $MX_2$, besides the common hexagonal forms, it presents a stable orthorhombic structure with highly in-plane anisotropic properties and giant negative Poisson's ratios. For $M_2X_3$, on the other hand, it presents no hexagonal but another orthorhombic structure with highly anisotropic mechanical and electronic features. These orthorhombic $MX_2$ and $M_2X_3$ are semiconducting with band gaps ranging from 1.05 to 2.40 eV, and they are hyperbolic materials operating in a broad range of the electromagnetic spectrum from infrared to ultraviolet. Moreover, by joint analysis of band gaps, band edges and optical absorption, $Ni_2Se_3$, $Pd_2S_3$ and orthorhombic $MX_2$ are found to be highly efficient for solar-driven photocatalytic water splitting.



## 1 Introduction

Two-dimensional (2D) transition metal chalcogenides (TMCs), including the transition metal dichalcogenides (for example, $MoS_2$, $MoSe_2$, $WS_2$, and $WSe_2$), have shown great potential in electronic and optical devices, such as high current on/off ratio field-effect transistors (FETs),[1,2] photodetectors[3,4] and valleytronic applications.[5,6] Most reported 2D TMCs have isotropic mechanical and electronic properties due to their highly symmetric structures. The symmetry of the lattice structure indeed plays a vital role in determining the electronic properties of materials. By lowering the symmetry of the structure, it is possible to induce strong in-plane anisotropic properties in 2D materials, as observed in puckered phosphorene,[7,8] group-IV monochalcogenides (SnS, SnSe, GeS, and GeSe),[9–11] and other 2D materials such as Sb and AsP.[12,13] As already reported, anisotropic properties have advantages for certain applications, such as polarized light detection devices and valleytronics.[14–16] Furthermore, the properties of anisotropy are highly related to hyperbolic materials, which have unique abilities for controlling light propagation.[17,18]

Recently, few-layer $PdSe_2$ has been successfully synthesized *via* mechanical exfoliation and selenization on the precursor Pd layer,[19–21] which has aroused great interest due to its ambient stability, high carrier mobility ($\sim$158 $cm^2 V^{-1} s^{-1}$) and in-plane anisotropic properties.[22] In contrast to its hexagonal form (Fig. 1(b)), the synthesized few-layer $PdSe_2$ forms an orthorhombic lattice with a puckered pentagonal structure, as illustrated in Fig. 1(c). Moreover, Li *et al.* revealed a much lower diffusion barrier of Se vacancies in $PdSe_2$ than that of S vacancy in $MoS_2$.[23] Further, Lin *et al.* demonstrated that the introduction of Se vacancy in few-layer $PdSe_2$ can enhance the interlayer interaction and decrease the Se/Pd element ratio, which creates a new structure form, *i.e.*, $Pd_2Se_3$,[24] as shown in Fig. 1(d). It is therefore highly desirable to look for other 2D TMCs with a similar structure to $PdSe_2$ or $Pd_2Se_3$, which may be stable and reveal the in-plane anisotropic properties.

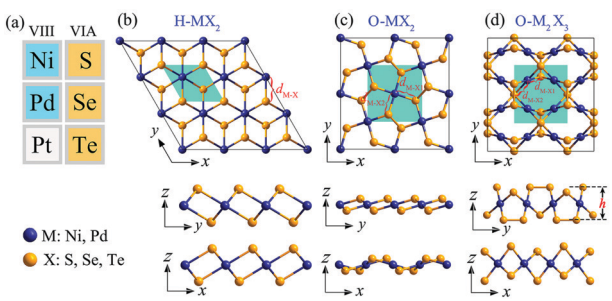


Fig. 1 (a) The VIII and VIA elements in the periodic table. Top and side views of (b) H-$MX_2$, (c) O-$MX_2$ and (d) O-$M_2X_3$, respectively. The green regions denote the unit cell.

[a] Key Laboratory of Artificial Micro- and Nano-structures of Ministry of Education and School of Physics and Technology, Wuhan University, Wuhan 430072, China. E-mail: s.yuan@whu.edu.cn
[b] Center for Quantum Computing, Peng Cheng Laboratory, Shenzhen 518055, China

† Electronic supplementary information (ESI) available. See DOI: 10.1039/c9tc04933a

Furthermore, one important application of 2D materials is photocatalytic water splitting, *i.e.*, converting solar energy into chemical energy without additional cost.[25–27] Since the discovery of $TiO_2$ as a photocatalyst in 1972,[28] more and more semiconductors have been proposed, including 2D semiconductors such as g-$C_3N_4$ and $MoS_2$.[29,30] Particularly, one or few-layer 2D semiconductors are indeed thin, with inherent merit as photocatalysts due to their extremely large specific surface area. In fact, an ideal photocatalyst should have two characters: (i) the band edge needs to straddle both the reduction potential of $H_2/H^+$ (−4.44 eV at pH = 0) and the oxidation potential of $H_2O/O_2$ (−5.67 eV at pH = 0); (ii) an appropriate optical gap to guarantee the absorption of the solar light. Once satisfying principle (i), the holes and electrons can drive both the oxidation and reduction reactions to generate $O_2$ and $H_2$ from aqueous solution. We will use these principles to look for possible photocatalysts from the 2D TMCs studied in this paper.

In this paper, we will perform a systematic study on 2D TMCs based on the VIII–VIA compounds in the form of $M_mX_n$, where M refers to the elements Ni and Pd, and X represents S, Se and Te. We will calculate the physical properties of eighteen 2D TMCs from first principles by using density functional theory (DFT). The structures of these materials are classified into three forms, namely, the hexagonal $MX_2$ (H-$MX_2$), the orthorhombic $MX_2$ (O-$MX_2$) and the orthorhombic $M_2X_3$ (O-$M_2X_3$). In the following, we will first present the details of the numerical methods in Section 2 and then show the main results in Section 3, including the stability, mechanical, electronic and optical properties of monolayer $M_mX_n$, and their potential applications in photocatalysis. Finally, we summarize our major findings in Section 4.

## 2 Computational methods

The electronic properties of TMCs are calculated from first-principles by using DFT as implemented in VASP code.[31] The Perdew–Burke–Ernzerhof (PBE) parametrized generalized gradient approximation (GGA) and projected augmented wave (PAW) are adopted to describe exchange correlation potential and ion–electron interaction.[32,33] The kinetic energy cutoff and *k*-point mesh of Brillouin zone (BZ) are set to 500 eV and 15 × 15 × 1,[34] respectively. A vacuum thickness of 20 Å is added to avoid the periodic interaction. Moreover, the energy convergence criterion and stress force are set to $10^{-5}$ eV and 0.01 eV Å$^{-1}$, respectively. For few-layer TMCs, the van der Waals (vdW) force is corrected by using a semi-empirical DFT-D2 method.[35,36] The spin–orbit coupling (SOC) is added into self-consistent calculations. Also, the corrected band structures are calculated by adopting the hybrid Heyd–Scuseria–Ernzerhof (HSE06) method.[37]

The thermal stability of monolayer TMCs is evaluated by using PHONOPY code based on density functional perturbation theory (DFPT) and the finite difference method.[38–40] We construct a 3 × 3 supercell and adopt a 5 × 5 × 1 *k*-point mesh to obtain force constants and the phonon spectrum. In order to eliminate the imaginary frequency, the highly accurate energy convergence criterion and stress force are set to $10^{-8}$ eV and $10^{-4}$ eV Å$^{-1}$, respectively.

## 3 Results and discussion

### 3.1 Structural stability

We firstly study the basic geometric structures and thermal stability of monolayer $M_mX_n$ (M = Ni, Pd; X = S, Se, Te). After fully optimizing the atomic positions, $M_mX_n$ stabilizes into three structural symmetries, as shown in Fig. 1, namely, the hexagonal H-$MX_2$, the orthorhombic O-$MX_2$, and the orthorhombic O-$M_2X_3$. All geometric structures are built up with three atomic layers as X–M–X, in which one M layer is sandwiched with two X layers. Each M atom binds six X atoms in H-$MX_2$ and four X atoms in O-$MX_2$ and O-$M_2X_3$. Detailed geometry analysis shows that the space groups of H-$MX_2$, O-$MX_2$ and O-$M_2X_3$ are *P*3*m*1 (No. 164), $P2_1/c$ (No. 14) and *Pmmn* (No. 59), respectively. In contrast to the common form of hexagonal H-$MX_2$, the space groups of O-$MX_2$ and O-$M_2X_3$ have much lower symmetry.

The relaxed structural parameters, such as lattice constants (*a* and *b*), bond length ($d_{M-X}$), and vertical height (*h*), are listed in Table 1. These results show clearly that when the atomic radius of element M (X) increases from Ni (S) to Pd (Te), all bond lengths within the same structural forms always increase. Comparing to the hexagonal structure of H-$MX_2$, the bond lengths in the two orthorhombic O-$MX_2$ and O-$M_2X_3$ are more close to each other, but the height, defined as the out of plane distance between the top and bottom X sub-layers, is totally different. Furthermore, for the O-$MX_2$ and O-$M_2X_3$ structures, there is a diversity of in-plane lattice constants along different crystal lines, originating from the bond length difference between $d_{M-X1}$ and $d_{M-X2}$, as illustrated in Fig. 1. These differences further break the geometry symmetry and induce subsequently anisotropic mechanical and optical properties, as we will explore in detail in the following.

The thermal stability of O-$MX_2$ and O-$M_2X_3$ is qualitatively examined by *ab initio* molecular dynamics simulations implemented in GULP.[41,42] Here, we skip the discussion of H-$MX_2$, as these common hexagonal structures have already been synthesized successfully.[43–45] In our stability analysis, the 3 × 3 supercell of monolayer TMCs is used, and the time interval and time step of the testing period are set to be 5 × $10^{-12}$ s and 1 × $10^{-15}$ s, respectively. Our results show that the total energy of each structure considered in O-$MX_2$ and O-$M_2X_3$ oscillates persistently around a fixed value during the whole simulation (see the data of 300 K presented in Fig. S1 and S2 of the ESI†). The stability of these structures is further conformed from the spectra of phonon dispersions shown in Fig. S3 and S4 of the ESI.† No negative acoustic branch is observed for all the structures considered in this paper. These results obtained from *ab initio* molecular dynamics simulations and phonon dispersions from first-principles indicate that monolayer O-$MX_2$ and O-$M_2X_3$ with M = Ni, Pd and X = S, Se, Te are all stable at room temperature. We will then continue the study by examining their mechanical and electronic properties, together with the forms of H-$MX_2$.

 

Table 1 Lattice constants ($a$ and $b$), bond length ($d_{M-X}$), vertical height ($h$), exfoliation energy ($E_{exf}$), band gaps from PBE ($E_{gap}^{PBE}$) and HSE06 ($E_{gap}^{HSE}$) methods without and with the SOC effects of monolayer TMCs

| | $a$ (Å) | $b$ (Å) | $d_{M-X}$ (Å) | $h$ (Å) | $E_{exf}$ (J m$^{-2}$) | $E_{gap}^{PBE}$ (eV) | $E_{gap}^{PBE-SOC}$ (eV) | $E_{gap}^{HSE}$ (eV) | $E_{gap}^{HSE-SOC}$ (eV) |
|---|---|---|---|---|---|---|---|---|---|
| H-$NiS_2$ | 3.348 | 3.348 | 2.258 | 2.330 | 0.474 | 0.61 | 0.57 | 1.10 | 1.04 |
| H-$NiSe_2$ | 3.547 | 3.547 | 2.390 | 2.467 | 0.656 | 0.21 | 0.05 | 0.58 | 0.42 |
| H-$NiTe_2$ | 3.787 | 3.787 | 2.576 | 2.721 | 0.582 | 0 | 0 | 0 | 0 |
| H-$PdS_2$ | 3.548 | 3.548 | 2.395 | 2.480 | 0.253 | 1.27 | 1.22 | 1.80 | 1.74 |
| H-$PdSe_2$ | 3.730 | 3.730 | 2.523 | 2.627 | 0.309 | 0.72 | 0.56 | 1.13 | 0.93 |
| H-$PdTe_2$ | 4.026 | 4.026 | 2.701 | 2.756 | 0.525 | 0.26 | 0 | 0.52 | 0.17 |
| O-$NiS_2$ | 5.215 | 5.326 | 2.172/2.182 | 1.149 | 0.279 | 0.82 | 0.81 | 2.40 | 2.39 |
| O-$NiSe_2$ | 5.512 | 5.702 | 2.305/2.314 | 1.368 | 0.343 | 1.02 | 0.99 | 2.27 | 2.27 |
| O-$NiTe_2$ | 5.955 | 6.261 | 2.489/2.498 | 1.552 | 0.411 | 0.95 | 0.91 | 1.89 | 1.85 |
| O-$PdS_2$ | 5.472 | 5.571 | 2.328/2.339 | 1.267 | 0.412 | 1.18 | 1.15 | 2.14 | 2.13 |
| O-$PdSe_2$ | 5.744 | 5.919 | 2.452/2.462 | 1.488 | 0.328 | 1.36 | 1.34 | 2.16 | 2.15 |
| O-$PdTe_2$ | 6.146 | 6.439 | 2.625/2.631 | 1.693 | 0.405 | 1.27 | 1.24 | 1.90 | 1.83 |
| O-$Ni_2S_3$ | 5.239 | 5.57 | 2.190/2.256 | 3.438 | 0.217 | 0.38 | 0.36 | 1.77 | 1.77 |
| O-$Ni_2Se_3$ | 5.423 | 5.926 | 2.310/2.383 | 3.704 | 0.295 | 0.37 | 0.35 | 1.61 | 1.59 |
| O-$Ni_2Te_3$ | 5.499 | 6.737 | 2.488/2.571 | 4.105 | 0.389 | 0.30 | 0.29 | 1.05 | 0.63 |
| O-$Pd_2S_3$ | 5.773 | 5.907 | 2.341/2.427 | 3.582 | 0.209 | 0.45 | 0.44 | 1.50 | 1.49 |
| O-$Pd_2Se_3$ | 5.976 | 6.114 | 2.455/2.539 | 3.842 | 0.276 | 0.42 | 0.41 | 1.39 | 1.38 |
| O-$Pd_2Te_3$ | 6.122 | 6.608 | 2.622/2.696 | 4.228 | 0.365 | 0.60 | 0.58 | 1.24 | 1.12 |

In addition, mechanical exfoliation is the most common approach to cleave 2D materials from their bulk counterparts,[46] whose feasibility can be evaluated by the exfoliation energy. Taking graphite as an example, the calculated exfoliation energy is 0.32 J m$^{-2}$. As shown in Table 1, most TMCs have similar or even lower exfoliation energies compared to graphite, indicating that in principle their monolayer can be exfoliated mechanically from their bulk similar to graphene from graphite. In fact, O-$PdSe_2$ has been synthesized experimentally *via* mechanical exfoliation.

### 3.2 Mechanical properties

The three forms of monolayer TMCs considered in this paper present totally different lattice structures. Materials belonging to the same forms of TMCs may have similar properties originating from the characters of their space group, but those from different forms should have significant differences in their physical properties. As one of the most important mechanical properties, we examine the first Young's modulus $Y(\theta)$ and Poisson's ratio $\nu(\theta)$ in the following.

Based on Hooke's law, the relationship between stiffness constants and modulus is given by

$$\begin{bmatrix} \sigma_{xx} \\ \sigma_{yy} \\ \sigma_{xy} \end{bmatrix} = \begin{bmatrix} C_{11} & C_{12} & 0 \\ C_{12} & C_{22} & 0 \\ 0 & 0 & C_{66} \end{bmatrix} \begin{bmatrix} \varepsilon_{xx} \\ \varepsilon_{yy} \\ 2\varepsilon_{xy} \end{bmatrix}, \quad (1)$$

where the in-plane stiffness tensor $C_{ij}$ ($i, j$ = 1, 2, 6) is equal to the second partial derivative of strain energy $E_s$, which is obtained by

$$E_s = \frac{1}{2}C_{11}\varepsilon_{xx}^2 + \frac{1}{2}C_{22}\varepsilon_{yy}^2 + C_{12}\varepsilon_{xx}\varepsilon_{yy} + 2C_{66}\varepsilon_{xy}^2, \quad (2)$$

where the tensile strain is defined as $\varepsilon = (a - a_0)/a_0$; here, $a$ and $a_0$ are strained and unstrained lattice constants, respectively. Young's modulus $Y$ and Poisson's ratio $\nu$ can be expressed as functions of the in-plane stiffness tensors as[47]

$$Y_x = (C_{11}C_{22} - C_{12}^2)/C_{22}, \quad Y_y = (C_{11}C_{22} - C_{12}^2)/C_{11}, \quad (3)$$

$$\nu_x = C_{12}/C_{22}, \quad \nu_y = C_{12}/C_{11}, \quad (4)$$

In fact, the anisotropic mechanical feature can be further checked by calculating the orientation-dependent Young's modulus $Y$ and Poisson's ratio $\nu$, which are expressed as[48]

$$Y(\theta) = \frac{C_{11}C_{22} - C_{12}^2}{C_{11}s^4 + C_{22}c^4 + \left(\frac{(C_{11}C_{22} - C_{12}^2)}{C_{66}} - 2C_{12}\right)s^2c^2}, \quad (5)$$

$$\nu(\theta) = \frac{C_{12}(s^4 + c^4) - \left(C_{11} + C_{22} - \frac{(C_{11}C_{22} - C_{12}^2)}{C_{66}}\right)s^2c^2}{C_{11}s^4 + C_{22}c^4 + \left(\frac{(C_{11}C_{22} - C_{12}^2)}{C_{66}} - 2C_{12}\right)s^2c^2}, \quad (6)$$

where $s = \sin\theta$ and $c = \cos\theta$.

The in-plane stiffness tensors $C_{ij}$ are obtained from a series of strain $|\varepsilon| \leq 2\%$ and a step of 0.5%. All in-plane stiffness tensors $C_{ij}$ fitted from eqn (2) for eighteen monolayer TMCs are collected in Table S1 of the ESI.† The orientation-dependent Young's modulus $Y(\theta)$ and Poisson's ratio $\nu(\theta)$ calculated by using eqn (5) and (6) are plotted in Fig. 2. It is clear that all structures in the H-$MX_2$ form are isotropic as both Young's modulus $Y(\theta)$ and Poisson's ratio $\nu(\theta)$ remain as constants when varying $\theta$; but the other two structures, O-$MX_2$ and O-$M_2X_3$, are highly anisotropic with clear angle-dependent mechanical properties.

Particularly, the Young's modulus of O-$MX_2$ increases monotonically from a minimum Young's modulus along the $x$ direction ($\theta = 0^\circ$) to a maximum value along the $y$ direction ($\theta = 90^\circ$). However, the maximum and minimum values of O-$M_2X_3$ are

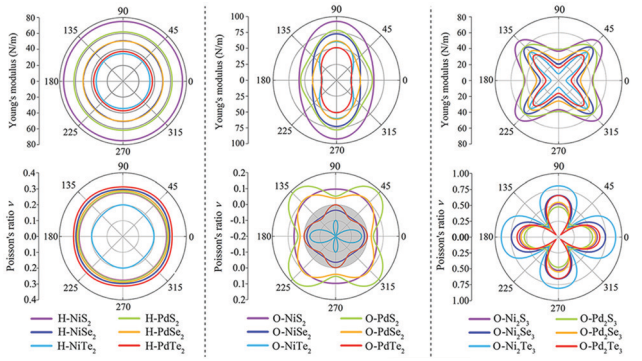


Fig. 2 Calculated orientation-dependent Young's modulus $Y(\theta)$ (top panel) and Poisson's ratio $\nu(\theta)$ (bottom panel) for H-$MX_2$, O-$MX_2$ and O-$M_2X_3$, respectively. The grey region denotes negative Poisson's ratio.

located at 45° and 0° (90°), respectively. For the same element M (*i.e.*, Ni, Pd), Young's modulus decreases as X changes from S to Te due to the increment of the M–X bond strength. Furthermore, our calculations show that O-$Ni_2Te_3$ and O-$Pd_2Te_3$ have ultra-low Young's modulus values ($<20$ N m$^{-1}$), which are even lower than that of monolayer graphene (340 N m$^{-1}$) and $MoS_2$ (125 N m$^{-1}$),[49,50] indicating their enormous potential in flexible devices.

For Poisson's ratio, besides the quite interesting anisotropic feature that appeared for O-$MX_2$ and O-$M_2X_3M_2X_3$, our calculations show that three monolayer TMCs, O-$NiSe_2$, O-$NiTe_2$ and O-$PdTe_2$, present negative Poisson's ratios. The absolute value of negative Poisson's ratio obtained among these materials is $-0.228$ in O-$NiTe_2$ along 56° to the $x$ axis (see Fig. 1(c)). A material with a negative Poisson's ratio exhibits an interesting auxetic effect, *i.e.*, it expands along one direction if stretched along another direction. Auxetic materials are highly desirable for tissue engineering, bulletproof vests and many other medical applications. As a comparison to existing auxetic 2D materials such as borophene, penta-graphene, and tinselenidene, we collect and list their Poisson's ratios together with the current values of O-$NiSe_2$, O-$NiTe_2$ and O-$PdTe_2$ in Table 2. O-$NiTe_2$ has the lowest Poisson's ratio among the three studied materials, and it is comparable to other reported auxetic 2D materials.

Actually, the nature of isotropic or anisotropic mechanical properties can be explained by analyzing the charge densities obtained from first-principles. Here, we use the case of M = Ni and X = S as an example to compare the charge distributions in

Table 2 The negative Poisson's ratios $\nu$ in $x$ and $y$ directions and its maximum value $\nu_{max}$ for other 2D materials

| System | $\nu_x$ | $\nu_y$ | $\nu_{max}$ |
|---|---|---|---|
| O-$NiSe_2$ | −0.018 | −0.036 | −0.050 |
| O-$NiTe_2$ | −0.037 | −0.100 | −0.228 |
| O-$PdTe_2$ | −0.001 | −0.002 | −0.058 |
| Borophene[47] | −0.022 | −0.009 | — |
| $\delta$-Silica[51] | −0.123 | −0.112 | — |
| Penta-graphene[52] | −0.068 | −0.068 | — |
| $Be_5C_2$[53] | −0.041 | −0.16 | — |
| $\delta$-AsN[54] | −0.177 | −0.068 | −0.296 |
| Tinselenidene[55] | −0.171 | 0.46 | — |

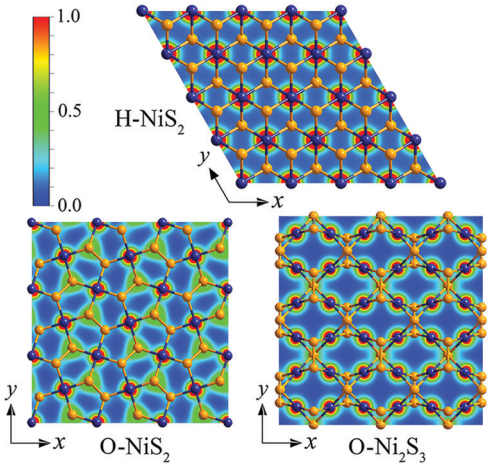


Fig. 3 The distribution of the charge density in the ground states of H-$NiS_2$, O-$NiS_2$ and O-$Ni_2S_3$. The color indicates the relative amplitude of the local densities.

the three different structural forms. As plotted in Fig. 3, the charge densities of H-$NiS_2$ are localized isotropically around Ni atoms. In contrast, the charge densities of O-$NiS_2$ and O-$Ni_2S_3$ are not uniformly distributed, but form patterns continuing along one crystal line. To be more precise, for O-$NiS_2$, the extended pattern is along the $y$ direction, and for O-$Ni_2S_3$, it is along the diagonal direction. This is, indeed, consistent with the calculated Young's modulus, in which the maximum values appear in a continuous pattern. The electron orbitals are hybridized more strongly along these directions, leading to a larger overlap of wave functions and larger bonding strength, and subsequently higher stiffness.

### 3.3 Electronic properties

In this section, we study the electronic properties of monolayer TMCs. We firstly perform band structure calculations by using PBE. The results show that most materials considered in our paper are semiconductors (see details in the ESI†). As the PBE method usually underestimates the band gap of a semiconductor, we performed DFT calculations in VASP with the more accurate HSE06 method and show the obtained band structures with projected densities in Fig. 4. The HSE06 results are similar to those in PBE, and all monolayer TMCs are semiconductors with indirect band gaps, except H-$NiTe_2$ which is a metal. Detailed analysis shows that, for H-$MX_2$, the conduction band minimum (CBM) and the valence band maximum (VBM) are mainly attributed to element X; for O-$MX_2$ and O-$M_2X_3$, the CBM and VBM originate from both compounds of M and X. The values of band gap obtained from both PBE and HSE06 are listed in Table 1. This indicates that for the materials in the same structural form, the band gaps always decrease as the element X varies from S to Te, which is similar to that observed in $MoX_2$ and $WX_2$ (X = S, Se and Te).[56] As there are relatively heavy elements in the considered TMCs, it is worth checking also the effects of the SOC. From the results obtained with or without SOC in PBE and HSE06 (see Fig. S6 and S7 in ESI†), we confirm

 

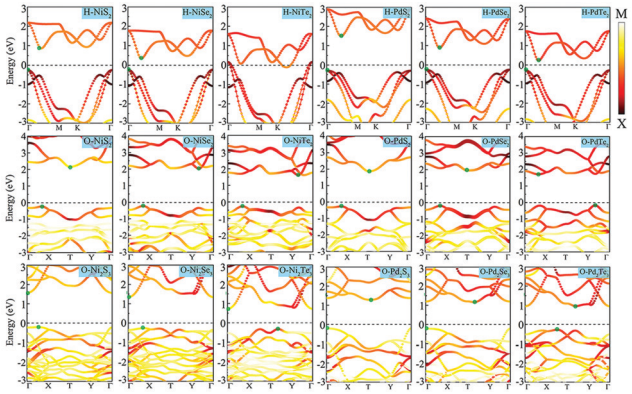

Fig. 4 The HSE06 projected band structures of eighteen monolayer TMCs.

that the SOC interaction is overall negligible for most materials considered in our paper, except H-$NiTe_2$ and H-$PdTe_2$. In these two materials, there is clearly large splitting of energy bands due to SOC, especially around the $\Gamma$ point. However, this splitting will not change qualitatively the properties studied in this paper, therefore we will neglect SOC in the following discussions.

All three forms of TMCs present stable multilayer structures stacked along the direction perpendicular to their plane. In Fig. 5(a), we show the atomic structures of stacked trilayer TMCs. The stacking sequence of H-$MX_2$, O-$MX_2$ and O-$M_2X_3$ is AAA stacking. We calculate further the electronic properties of multilayer TMCs by using relaxed structures, as shown in Fig. 5(a), and we present the main results in Fig. 5(b). Here, we consider mainly the thickness-dependence of the electronic properties of the multilayer structure, and show the values of

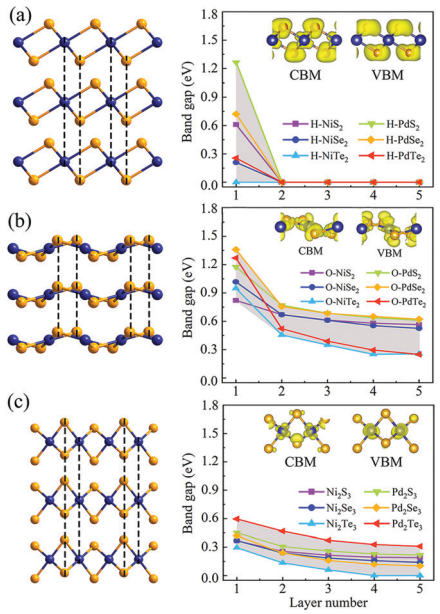

Fig. 5 Atomic structures of few-layer TMCs and layer number-dependent PBE band gaps for (a) H-$MX_2$, (b) O-$MX_2$ and (c) O-$M_2X_3$, respectively. The insets are band decomposed charge densities of monolayer H-$NiS_2$, O-$NiS_2$ and $Ni_2S_2$ for CBM and VBM, respectively.

band gap with different numbers of layers ranging from 1 to 5. As is well known, the interlayer vdW interaction, which is absent in a monolayer, plays a vital role in determining the properties of multilayer 2D materials, especially at low energy around the Fermi level. In general, the interlayer vdW interaction will lower the band gap for semiconducting 2D materials, because of the hybridization of the bands between neighboring layers. This is indeed also the case for TMCs considered in our paper. In particular, once H-$MX_2$ becomes a bilayer, its band gap promptly decreases to zero (see the results shown in Fig. S8, ESI†), indicating that it gives a fierce response to the thickness. For O-$MX_2$ and O-$M_2X_3$, their band gaps keep decreasing when adding more layers, but gradually. Specifically, the variation ranges of band gaps are 0–1.27 eV, 0.26–1.36 eV and 0–0.60 eV for H-$MX_2$, O-$MX_2$ and O-$M_2X_3$, respectively. To further explore the origin of the relationship between the band gaps and the interlayer coupling, Fig. 5 shows the band decomposed charge densities of CBM and VBM in the monolayer. For H-$NiS_2$, O-$NiS_2$ and O-$Ni_2S_3$, charge densities of CBM and VBM are distributed among outside S atoms, Ni–S bonds and inside Ni atoms, respectively. When the monolayers are stacked together, the few-layer H-$NiS_2$ and O-$Ni_2S_3$ have maximum (minimum) interlayer charge overlapping, leading to maximum (minimum) changes of band gap.

### 3.4 Photocatalysis and light absorption

Most monolayer TMCs considered in this paper are semiconducting with energy gaps ranging from 0.52 to 2.40 eV according to HSE06 calculations, providing a wide range of candidates for different optical applications. The main concern in the following is to study their potential applications in photocatalytic water splitting, *i.e.*, converting solar energy into chemical energy without additional cost.[25–28] As designing principles, a highly efficient water splitting photocatalyst should hold two characters: (i) a band gap of about 2.0 eV for the harvesting of solar energy; (ii) band edges (CBM and VBM) straddling both the reduction potential of $H_2/H^+$ (−4.44 eV, pH = 0) and the oxidation potential of $H_2O/O_2$ (−5.67 eV, pH = 0). Here, hydrogen production *via* photocatalytic water splitting needs ultrahigh solar energy harvesting to drive the oxidation and reduction reactions.

To be more precise, in the oxidation reaction, the holes are used to generate $O_2$:

$$4h^+ + 2H_2O \rightarrow O_2 + 4H^+, \quad (7)$$

meanwhile, the excited electrons take part in the hydrogen reduction reaction to produce $H_2$:

$$4e^- + 4H_2O \rightarrow 2H_2 + 4OH^-, \quad (8)$$

In fact, the redox potentials of water are related to the pH of the aqueous solution. According to the Nernst equation,[58–60] the water redox potentials and the value of pH satisfy the following relation:

$$E^{pH} = E^{pH=0} - 0.059 \times pH, \quad (9)$$

which means that the redox potentials of water increase linearly with pH by a factor of 0.059 eV per pH.

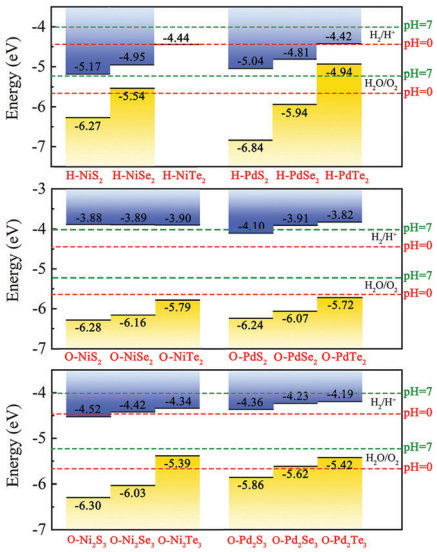


Fig. 6 Band alignments of monolayer H-$MX_2$, O-$MX_2$ and O-$M_2X_3$ with respect to the redox potentials of water.

Here, in Fig. 6, by adopting the HSE06 method, the accurate band alignments of monolayer TMCs are obtained. For H-$MX_2$, the CBM and VBM never meet the requirement of redox potentials at pH = 0 or 7, indicating that they cannot be used for achieving water splitting. For O-$MX_2$, the CBM and VBM are always higher and lower than the reduction and oxidation potentials at pH = 0, respectively, implying that they have an inherent advantage in realizing water splitting. When the pH of the aqueous solution increases to 7, only the CBM of monolayer O-$PdS_2$ fails in producing $H_2$. For O-$M_2X_3$, both O-$Ni_2Se_3$ and O-$Pd_2S_3$ meet the redox potentials at pH = 0, but they fail in realizing water splitting at pH = 7. To further analyse the ability of water splitting, the kinetic overpotentials $\Delta E_C$ and $\Delta E_V$ (the difference between band edge and redox potential) are obtained, which can represent properly the efficiency of driving the redox reaction (see details in Table S2 of the ESI†). This shows that when the pH of the aqueous solution increases, $\Delta E_C$ decreases and $\Delta E_V$ increases. The pH value-dependent kinetic overpotential shows a tunable ability of $H_2$ production. These results imply that O-$MX_2$, O-$Ni_2Se_3$ and O-$Pd_2S_3$ are possible photocatalysts for water splitting at specific pH values of aqueous solution.

To investigate the actual performance, we further need to consider the sunlight harvesting of these candidates by calculating their optical absorption coefficients. Using the GW approximation in conjunction with the Bethe-Salpeter equation (BSE),[61,62] the light absorbance is obtained and plotted in Fig. 7. Here, we include the electron–hole interaction in the optical calculation, as the charge screening effect is much weaker in two-dimension compared to three-dimension due to the absence of screening along the out-of-plane direction. The solar energy is distributed as infrared, visible and ultraviolet light by about 43%, 50% and 7%, respectively. Fig. 7 shows that O-$MX_2$, O-$Ni_2Se_3$ and O-$Pd_2S_3$ have ultrahigh absorption coefficients within both visible (400–760 nm) and ultraviolet ranges (<760 nm), indicating their excellent harvesting of the solar energy. As a comparison, we perform optical calculations of widely used intrinsic silicon, and other 2D semiconductor photocatalysts, including g-$C_3N_4$ and $MoS_2$. When the wavelength is longer than 400 nm, the absorption coefficients of our TMC candidates are much higher than all other compared materials; for example, they are about ten times higher than the value of intrinsic silicon. Specifically, O-$Ni_2Se_3$ shows high and constant absorption over the entire energy range of sunlight. Our results identify that O-$MX_2$, O-$Ni_2Se_3$ and O-$Pd_2S_3$ have large absorption coefficients from visible to ultraviolet light and provide congenital advantages for applications as a photocatalyst. Furthermore, monolayer O-$MX_2$, O-$Ni_2Se_3$ and O-$Pd_2S_3$ present highly anisotropic optical properties, consistent with their mechanical properties. These materials can be used also as polarization-dependent photodetectors, similar to those proposed for other 2D materials such as black phosphorus.[63]

In addition, the strong in-plane anisotropy of TMCs suggests their potential as natural hyperbolic materials, offering possibilities for manipulating directional plasmons, light emitters, superlensing effects, *etc.*[18,64] A hyperbolic region appears when[65]

$$\mathrm{Re}\,\varepsilon_x(\omega) \times \mathrm{Re}\,\varepsilon_y(\omega) < 0 \qquad (10)$$

where $\mathrm{Re}\,\varepsilon_x(\omega)$ and $\mathrm{Re}\,\varepsilon_y(\omega)$ are real parts of dielectric functions along two orthogonal in-plane directions, as defined in Fig. 3.

Taking monolayer O-$NiS_2$ and O-$Ni_2S_3$ as examples, we calculate their complex dielectric functions $\varepsilon_x(\omega)$ and $\varepsilon_y(\omega)$ from first-principles with the GW + BSE method,[61,62] and plot them in Fig. 8(a) and (b). This shows that the hyperbolic region

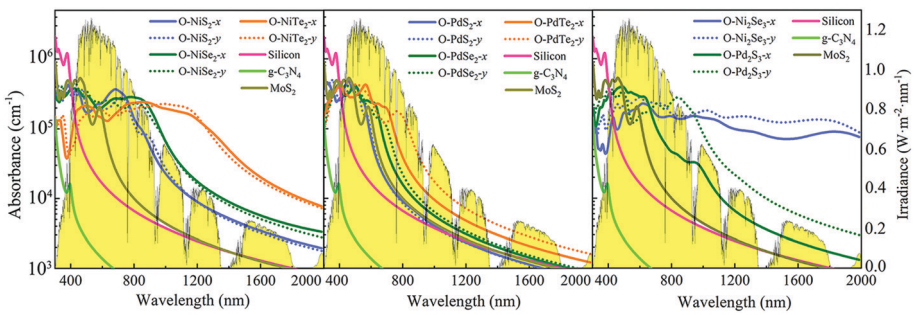


Fig. 7 The absorption coefficients of monolayer O-$MX_2$, O-$Ni_2Se_3$ and O-$Pd_2S_3$, respectively, calculated with GW-BSE. The yellow background denotes the reference solar spectral irradiance in incident AM1.5G solar flux.[57]

 

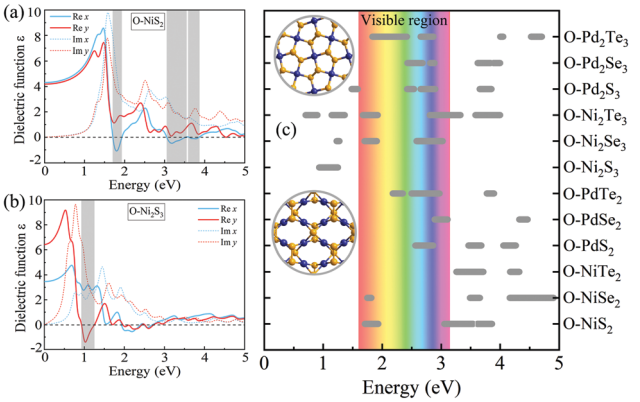


Fig. 8 Real and imaginary parts of complex dielectric functions of monolayer (a) O-$NiS_2$ and (b) O-$Ni_2S_3$. The grey shaded region shows the hyperbolic region. (c) The hyperbolic region marked in grey of monolayer O-$MX_2$ and O-$M_2X_3$. The visual spectrum is indicated in color.

emerges in both materials, but at different energies. To be more precise, for O-$NiS_2$, the hyperbolic regions appear within the range of visible light (1.70–1.93 eV) and ultraviolet light (3.06–3.87 eV), and for O-$Ni_2S_3$, it appears in the infrared (0.93–1.25 eV) region. A systematic study of the energy dependent complex dielectric functions of orthorhombic TMCs shows that all O-$MX_2$ and O-$M_2X_3$ considered in our paper are hyperbolic in certain energy regions below 5 eV. These regions are collected and labeled in Fig. 8(c), covering the infrared, visible and ultraviolet light ranges. Our results indicate that O-$MX_2$ and O-$M_2X_3$ are hyperbolic materials and for applications with a certain wavelength, one can select one of them with matched hyperbolic regions. Furthermore, as these two-dimensional materials are atom-thin, their electronic structures and optical properties can be manipulated by electrostatic bias and external stain, and we expect that the hyperbolic regions of O-$MX_2$ and O-$M_2X_3$ are highly tunable. A detailed study of electronically and mechanically engineering the hyperbolic regions of these orthorhombic TMCs is worth addressing separately in future work.

## 4 Conclusion

In conclusion, we have studied three forms of monolayer transition metal chalcogenides H-$MX_2$, O-$MX_2$ and O-$M_2X_3$ (M = Ni, Pd; X = S, Se, Te). We systematically examined their structural, mechanical, electronic and optical characteristics *via* first-principle calculations. All these structures are stable at room temperature, verified by time-dependent *ab initio* molecular dynamics simulations and their phonon dispersion. The calculated mechanical properties also show that H-$MX_2$ is isotropic, while O-$MX_2$ and O-$M_2X_3$ present highly in-plane anisotropy due to their reduced lattice symmetry. In particular, all O-$MX_2$ and O-$M_2X_3$ considered in our paper are hyperbolic in certain regions covering the infrared, visible and ultraviolet light ranges. Furthermore, O-$MX_2$ shows great auxeticity with giant negative in-plane Poisson's ratios, which are comparable to other known two-dimensional materials. Hence, O-$MX_2$ has an ultra-low Young's modulus. By calculating the band alignments and light absorption coefficients, we concluded that O-$MX_2$, O-$Ni_2Se_3$ and O-$Pd_2S_3$ can be used as flexible water splitting photocatalysts within visible and ultraviolet light regions, because of their suitable band gaps, band edges and ultrahigh sunlight absorption.

## Conflicts of interest

There are no conflicts to declare.

## Acknowledgements

This work is supported by the National Key R&D Program of China (Grant No. 2018FYA0305800). Numerical calculations presented in this paper have been performed on a supercomputing system in the Supercomputing Center of Wuhan University.

## Notes and references

1 B. Radisavljevic, A. Radenovic, J. Brivio, V. Giacometti and A. Kis, *Nat. Nanotechnol.*, 2011, **6**, 147–150.
2 Q. H. Wang, K. Kalantar-Zadeh, A. Kis, J. N. Coleman and M. S. Strano, *Nat. Nanotechnol.*, 2012, **7**, 699–712.
3 O. Lopez-Sanchez, D. Lembke, M. Kayci, A. Radenovic and A. Kis, *Nat. Nanotechnol.*, 2013, **8**, 497–501.
4 F. H. L. Koppens, T. Mueller, P. Avouris, A. C. Ferrari, M. S. Vitiello and M. Polini, *Nat. Nanotechnol.*, 2014, **9**, 780–793.
5 K. F. Mak, K. He, J. Shan and T. F. Heinz, *Nat. Nanotechnol.*, 2012, **7**, 494–498.
6 H. Zeng, J. Dai, W. Yao, D. Xiao and X. Cui, *Nat. Nanotechnol.*, 2012, **7**, 490–493.
7 L. Li, Y. Yu, G. J. Ye, Q. Ge, X. Ou, H. Wu, D. Feng, X. H. Chen and Y. Zhang, *Nat. Nanotechnol.*, 2014, **9**, 372–377.
8 J. Qiao, X. Kong, Z.-X. Hu, F. Yang and W. Ji, *Nat. Commun.*, 2014, **5**, 4475.
9 L. C. Gomes and A. Carvalho, *Phys. Rev. B: Condens. Matter Mater. Phys.*, 2015, **92**, 085406.
10 P. Z. Hanakata, A. Carvalho, D. K. Campbell and H. S. Park, *Phys. Rev. B*, 2016, **94**, 035304.
11 L. Xu, M. Yang, S. J. Wang and Y. P. Feng, *Phys. Rev. B*, 2017, **95**, 235434.
12 S. Zhang, S. Guo, Z. Chen, Y. Wang, H. Gao, J. Gómez-Herrero, P. Ares, F. Zamora, Z. Zhu and H. Zeng, *Chem. Soc. Rev.*, 2018, **47**, 982–1021.
13 S. Guo, Y. Zhang, Y. Ge, S. Zhang, H. Zeng and H. Zhang, *Adv. Mater.*, 2019, **31**, 1902352.
14 H. Tian, J. Tice, R. Fei, V. Tran, X. Yan, L. Yang and H. Wang, *Nano Today*, 2016, **11**, 763–777.
15 L. Kou, C. Chen and S. C. Smith, *J. Phys. Chem. Lett.*, 2015, **6**, 2794–2805.
16 X. Wang, A. M. Jones, K. L. Seyler, V. Tran, Y. Jia, H. Zhao, H. Wang, L. Yang, X. Xu and F. Xia, *Nat. Nanotechnol.*, 2015, **10**, 517–521.
17 S. Guan, S. Y. Huang, Y. Yao and S. A. Yang, *Phys. Rev. B*, 2017, **95**, 165436.

18 M. N. Gjerding, R. Petersen, T. G. Pedersen, N. A. Mortensen and K. S. Thygesen, *Nat. Commun.*, 2017, **8**, 320.
19 E. Li, D. Wang, P. Fan, R. Zhang, Y.-Y. Zhang, G. Li, J. Mao, Y. Wang, X. Lin, S. Du and H.-J. Gao, *Nano Res.*, 2018, **11**, 5858–5865.
20 W. L. Chow, P. Yu, F. Liu, J. Hong, X. Wang, Q. Zeng, C.-H. Hsu, C. Zhu, J. Zhou, X. Wang, J. Xia, J. Yan, Y. Chen, D. Wu, T. Yu, Z. Shen, H. Lin, C. Jin, B. K. Tay and Z. Liu, *Adv. Mater.*, 2017, **29**, 1602969.
21 L.-H. Zeng, D. Wu, S.-H. Lin, C. Xie, H.-Y. Yuan, W. Lu, S. P. Lau, Y. Chai, L.-B. Luo, Z.-J. Li and Y. H. Tsang, *Adv. Funct. Mater.*, 2019, **29**, 1806878.
22 A. D. Oyedele, S. Yang, L. Liang, A. A. Puretzky, K. Wang, J. Zhang, P. Yu, P. R. Pudasaini, A. W. Ghosh, Z. Liu, C. M. Rouleau, B. G. Sumpter, M. F. Chisholm, W. Zhou, P. D. Rack, D. B. Geohegan and K. Xiao, *J. Am. Chem. Soc.*, 2017, **139**, 14090–14097.
23 G. D. Nguyen, L. Liang, Q. Zou, M. Fu, A. D. Oyedele, B. G. Sumpter, Z. Liu, Z. Gai, K. Xiao and A.-P. Li, *Phys. Rev. Lett.*, 2018, **121**, 086101.
24 J. Lin, S. Zuluaga, P. Yu, Z. Liu, S. T. Pantelides and K. Suenaga, *Phys. Rev. Lett.*, 2017, **119**, 016101.
25 A. Iwase, Y. H. Ng, Y. Ishiguro, A. Kudo and R. Amal, *J. Am. Chem. Soc.*, 2011, **133**, 11054–11057.
26 K. Maeda and K. Domen, *J. Phys. Chem. Lett.*, 2010, **1**, 2655–2661.
27 P. Wang, B. Huang, X. Qin, X. Zhang, Y. Dai, J. Wei and M.-H. Whangbo, *Angew. Chem., Int. Ed.*, 2008, **47**, 7931–7933.
28 A. Fujishima and K. Honda, *Nature*, 1972, **238**, 37–38.
29 Q. Lu, Y. Yu, Q. Ma, B. Chen and H. Zhang, *Adv. Mater.*, 2016, **28**, 1917–1933.
30 Y. Zhang, J. Liu, G. Wu and W. Chen, *Nanoscale*, 2012, **4**, 5300.
31 G. Kresse and J. Furthmüller, *Phys. Rev. B: Condens. Matter Mater. Phys.*, 1996, **54**, 11169–11186.
32 P. E. Blöchl, *Phys. Rev. B: Condens. Matter Mater. Phys.*, 1994, **50**, 17953–17979.
33 J. P. Perdew, K. Burke and M. Ernzerhof, *Phys. Rev. Lett.*, 1996, **77**, 3865–3868.
34 H. J. Monkhorst and J. D. Pack, *Phys. Rev. B: Solid State*, 1976, **13**, 5188–5192.
35 S. Grimme, *J. Comput. Chem.*, 2006, **27**, 1787–1799.
36 T. Kerber, M. Sierka and J. Sauer, *J. Comput. Chem.*, 2008, **29**, 2088–2097.
37 J. Heyd, J. E. Peralta, G. E. Scuseria and R. L. Martin, *J. Chem. Phys.*, 2005, **123**, 174101.
38 X. Gonze, J.-C. Charlier, D. Allan and M. Teter, *Phys. Rev. B: Condens. Matter Mater. Phys.*, 1994, **50**, 13035–13038.
39 X. Gonze and C. Lee, *Phys. Rev. B: Condens. Matter Mater. Phys.*, 1997, **55**, 10355–10368.
40 P. Giannozzi, S. de Gironcoli, P. Pavone and S. Baroni, *Phys. Rev. B: Condens. Matter Mater. Phys.*, 1991, **43**, 7231–7242.
41 J. D. Gale and A. L. Rohl, *Mol. Simul.*, 2003, **29**, 291–341.
42 J. D. Gale, *J. Chem. Soc., Faraday Trans.*, 1997, **93**, 629–637.
43 J. Zhou, J. Lin, X. Huang, Y. Zhou, Y. Chen, J. Xia, H. Wang, Y. Xie, H. Yu, J. Lei, D. Wu, F. Liu, Q. Fu, Q. Zeng, C.-H. Hsu, C. Yang, L. Lu, T. Yu, Z. Shen, H. Lin, B. I. Yakobson, Q. Liu, K. Suenaga, G. Liu and Z. Liu, *Nature*, 2018, **556**, 355–359.
44 Y. Shao, S. Song, X. Wu, J. Qi, H. Lu, C. Liu, S. Zhu, Z. Liu, J. Wang, D. Shi, S. Du, Y. Wang and H.-J. Gao, *Appl. Phys. Lett.*, 2017, **111**, 113107.
45 P. Miró, M. Ghorbani-Asl and T. Heine, *Angew. Chem., Int. Ed.*, 2014, **53**, 3015–3018.
46 S. Zhang, Z. Yan, Y. Li, Z. Chen and H. Zeng, *Angew. Chem., Int. Ed.*, 2015, **54**, 3112–3115.
47 H. Zhong, K. Huang, G. Yu and S. Yuan, *Phys. Rev. B*, 2018, **98**, 054104.
48 V. Wang and W. T. Geng, *J. Phys. Chem. C*, 2017, **121**, 10224–10232.
49 C. Lee, X. Wei, J. W. Kysar and J. Hone, *Science*, 2008, **321**, 385–388.
50 D. Çakr, F. M. Peeters and C. Sevik, *Appl. Phys. Lett.*, 2014, **104**, 203110.
51 Z. Gao, X. Dong, N. Li and J. Ren, *Nano Lett.*, 2017, **17**, 772–777.
52 S. Zhang, J. Zhou, Q. Wang, X. Chen, Y. Kawazoe and P. Jena, *Proc. Natl. Acad. Sci. U. S. A.*, 2015, **112**, 2372–2377.
53 Y. Wang, F. Li, Y. Li and Z. Chen, *Nat. Commun.*, 2016, **7**, 11488.
54 W.-Z. Xiao, G. Xiao, Q.-Y. Rong and L.-L. Wang, *Phys. Chem. Chem. Phys.*, 2018, **20**, 22027–22037.
55 L.-C. Zhang, G. Qin, W.-Z. Fang, H.-J. Cui, Q.-R. Zheng, Q.-B. Yan and G. Su, *Sci. Rep.*, 2016, **6**, 19830.
56 J. Kang, S. Tongay, J. Zhou, J. Li and J. Wu, *Appl. Phys. Lett.*, 2013, **102**, 012111.
57 ASTM, G173-03, ASTM International, West Conshohocken, 2008, DOI: 10.1520/G0173-03R12.
58 J. M. Bolts and M. S. Wrighton, *J. Phys. Chem.*, 1976, **80**, 2641–2645.
59 X. Li, J. Yu, J. Low, Y. Fang, J. Xiao and X. Chen, *J. Mater. Chem. A*, 2015, **3**, 2485–2534.
60 T. A. Pham, D. Lee, E. Schwegler and G. Galli, *J. Am. Chem. Soc.*, 2014, **136**, 17071–17077.
61 M. Rohlfing and S. G. Louie, *Phys. Rev. B: Condens. Matter Mater. Phys.*, 2000, **62**, 4927–4944.
62 J. Deslippe, G. Samsonidze, D. A. Strubbe, M. Jain, M. L. Cohen and S. G. Louie, *Comput. Phys. Commun.*, 2012, **183**, 1269–1289.
63 Q. Guo, A. Pospischil, M. Bhuiyan, H. Jiang, H. Tian, D. Farmer, B. Deng, C. Li, S.-J. Han, H. Wang, Q. Xia, T.-P. Ma, T. Mueller and F. Xia, *Nano Lett.*, 2016, **16**, 4648–4655.
64 S. Guan, S. Y. Huang, Y. Yao and S. A. Yang, *Phys. Rev. B*, 2017, **95**, 165436.
65 E. van Veen, A. Nemilentsau, A. Kumar, R. Roldán, M. I. Katsnelson, T. Low and S. Yuan, *Phys. Rev. Appl.*, 2019, **12**, 014011.

 